

## Visualization of Electrode–Electrolyte Interfaces in LiPF<sub>6</sub>/EC/DEC Electrolyte for Lithium Ion Batteries via in Situ TEM

Zhiyuan Zeng,<sup>†</sup> Wen-I Liang,<sup>†,‡</sup> Hong-Gang Liao,<sup>†</sup> Huolin L. Xin,<sup>†</sup> Yin-Hao Chu,<sup>‡</sup> and Haimei Zheng<sup>\*,†,§</sup>

<sup>†</sup>Materials Sciences Division, Lawrence Berkeley National Laboratory, Berkeley, California 94720, United States

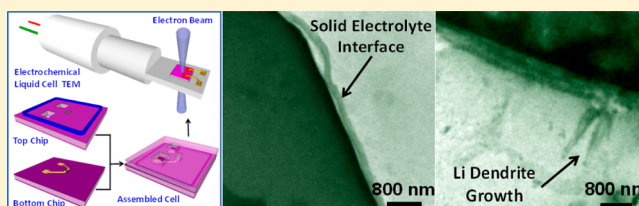
<sup>‡</sup>Department of Materials Science and Engineering, National Chiao Tung University, Hsinchu, 30010, Taiwan

<sup>§</sup>Department of Materials Science and Engineering, University of California, Berkeley, California 94720, United States

### S Supporting Information

**ABSTRACT:** We report direct visualization of electrochemical lithiation and delithiation of Au anodes in a commercial LiPF<sub>6</sub>/EC/DEC electrolyte for lithium ion batteries using transmission electron microscopy (TEM). The inhomogeneous lithiation, lithium metal dendritic growth, electrolyte decomposition, and solid–electrolyte interface (SEI) formation are observed in situ. These results shed lights on strategies of improving electrode design for reducing short-circuit failure and improving the performance of lithium ion batteries.

**KEYWORDS:** Liquid cell TEM, electrochemical liquid cell, lithium ion batteries, lithium dendrite, solid–electrolyte interface



During the charge–discharge of batteries, many electrochemical events can occur at the electrode–electrolyte interfaces such as lithium intercalation into the electrode, solid–electrolyte interface (SEI) formation, lithium dendritic growth at a high charge rate, and so on.<sup>1</sup> The dendritic growth of lithium metal on the electrode can lead to short-circuit and thus battery failure. To avoid dendritic growth, a slow charge rate has been incorporated, which is unfortunately one of the major issues of lithium ion batteries for powering electric vehicles. There have been a lot of efforts on the understanding of the mechanisms of lithium deposition on the electrode.<sup>2,3</sup> Arakawa et al. designed an optical microscope system to observe the morphology change of the lithium anode during charge cycles. By direct visualization, they showed that needle-like lithium was formed during charge/discharge processes, which led to “dead lithium”<sup>2</sup> under localized deposition or dissolution. The amount of needle-like lithium is inversely proportional to the discharge current density. On the other hand, a high rate discharge results in the recombination of separated lithium, which help to improve the cycle performance.<sup>2</sup> Later, Yamaki et al. reported that lithium dendrites are whiskers and they might grow from their base electrode during electrochemical deposition.<sup>3</sup> They proposed that the electro-deposited lithium may break the protective film and lithium whiskers grow as extrusions through the resulting hole.<sup>3</sup> The visualization by in situ optical microscopy has advanced our understanding of lithium dendrite formation significantly; however, the detailed growth mechanisms at the nanometer scale are still unclear.

Another important issue at the interface is the formation of SEI. SEI is a passivation interfacial film formed from the reduction of the solvent of the electrolyte, which is critical to the cycleability in lithium ion batteries. Lots of efforts have

been devoted to understand the nature of SEI, primarily by electrochemical tests and ex situ spectroscopy or microscopy techniques. The reported ex situ characterization techniques of SEI include atomic force microscopy (AFM), X-ray photoelectron spectroscopy (XPS), and scanning tunneling microscopy (STM), the use of vibrational spectroscopy such as FTIR or Raman spectroscopy, and so forth.<sup>4,5</sup> It is envisioned that SEI is a denser layer of inorganic components compact adhering to the electrode and a porous organic outlayer in contact with electrolyte.<sup>6</sup> However, it is unlikely that SEI preserves its pristine nature after steps of separation, washing, and isolation while performing ex situ studies since the SEI layer is highly sensitive to moisture, air, and other kinds of contaminations. For example, ROCO<sub>2</sub>Li reacts with water and decomposes into Li<sub>2</sub>CO<sub>3</sub>, CO<sub>2</sub>, and ROH;<sup>7</sup> ROCO<sub>2</sub>Li and ROli react with CO<sub>2</sub> and form Li<sub>2</sub>CO<sub>3</sub>,<sup>8</sup> and so on. The irreversible changes can occur on the SEI layer, leading to modification and degradation of SEI. Therefore, the ex situ characterization has inherent drawbacks in the study of SEI, especially the initial layer during the electrochemical process. In situ characterizations such as wide-angle X-ray scattering (WAXS), small-angle X-ray scattering (SAXS),<sup>9</sup> and neutron reflectometry<sup>10</sup> have recently been employed to monitor SEI formation. For instance, the changes in lattice parameter or the depth profile of the scattering length density can be analyzed.

In situ liquid cell transmission electron microscopy (TEM) allows imaging chemical reactions in liquids with high spatial resolution,<sup>11–15</sup> which opens the opportunity to address key

**Received:** October 20, 2013

**Revised:** December 29, 2013

**Published:** January 20, 2014

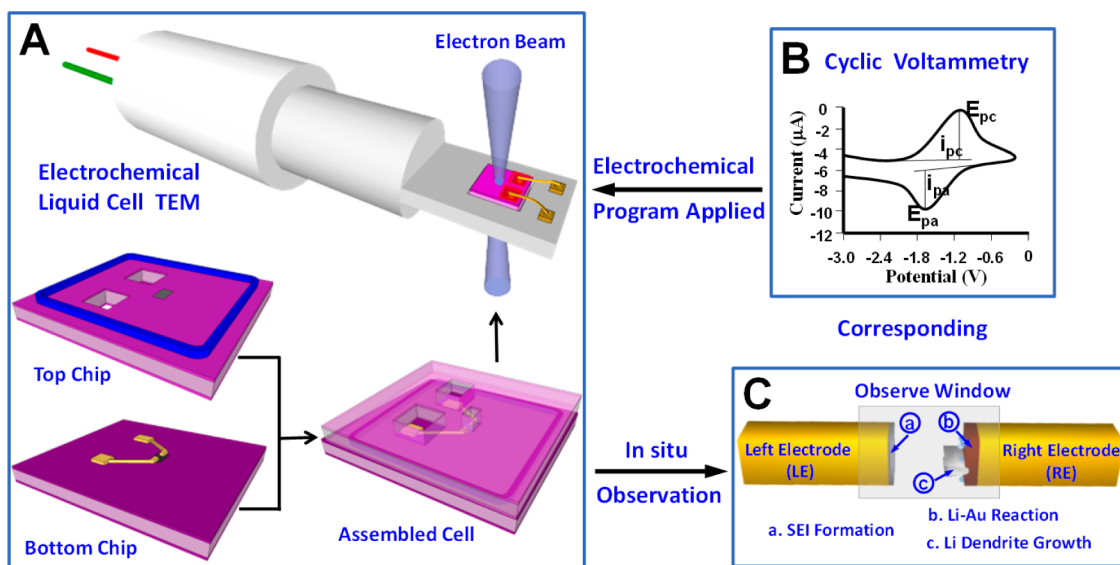


**Figure 1.** A scheme of in situ TEM observation of the electrochemical reaction using an electrochemical liquid cell: (A) a top microchip patterned with 150 nm thick metallic indium was covered and stuck onto bottom microchip with 120 nm thick gold electrode deposited on it, which is the assembled liquid cell for TEM visualization when embedded in a TEM holder; (B) cyclic voltammetry with a different voltage range applied to the electrochemical liquid cell TEM holder; (C) real time electrode–electrolyte interface reaction with commercial  $\text{LiPF}_6/\text{EC}/\text{DEC}$  electrolyte loaded in the liquid cell.

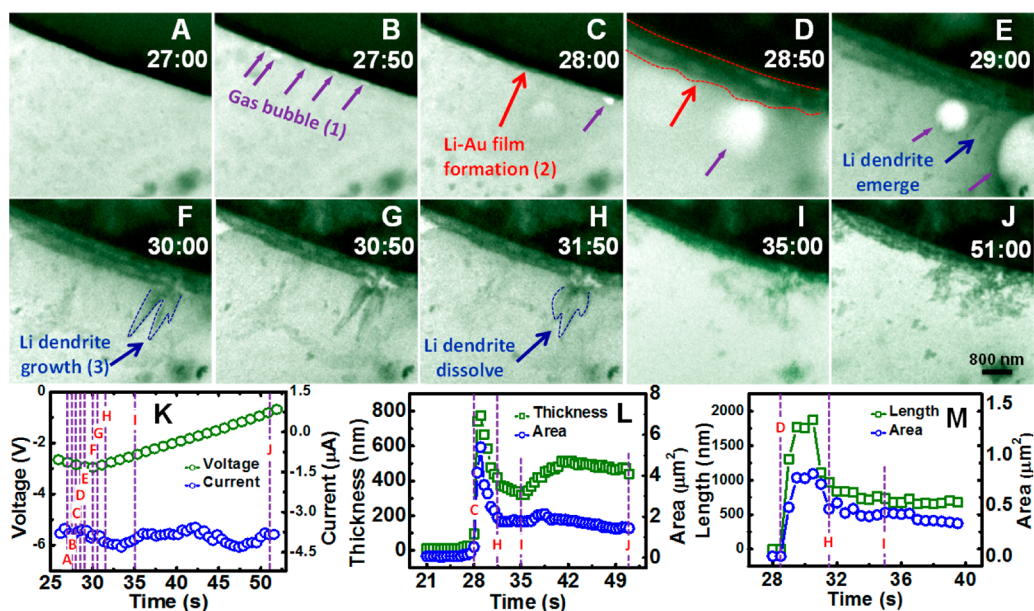


**Figure 2.** (A–J) Time evolution of the growth and dissolution of Li–Au alloy and lithium dendrite; (K) the corresponding applied electric potential and measured electric current from frame A to frame J; (L) plot of Li–Au layer thickness and area as a function of time; (M) dimension and area evolution of the lithium dendrite tip as a function of time during cyclic voltammetry in the voltage range of 0 to  $-3$  V at scan rate of  $0.1$  V/s.

questions on the electrode–electrolyte interfaces in a battery cell. Williamson et al.<sup>13</sup> and Radisic et al.<sup>14</sup> reported imaging electrochemical deposition of Cu clusters and polycrystalline Au using an electrochemical liquid cell. Chen et al.<sup>16</sup> achieved anisotropic electrodeposition of nickel nanograins with a homemade TEM cell. Our group demonstrated unique electrochemical growth of single crystal lead dendrites through nucleation, aggregation, alignment, and attachment of randomly oriented small grains.<sup>17</sup> Similarly, White et al.<sup>18</sup> conducted electrodeposition and stripping of lead on polycrystalline gold electrodes with a similar electrochemical cell set up. A series of in situ TEM experiments were conducted in a nanobattery cell,

such as electrochemical lithiation of  $\text{SnO}_2$  nanowire,<sup>19</sup> Si nanowires,<sup>20,21</sup> and nanospheres,<sup>22</sup> Si/CNF composite,<sup>23</sup> and other kinds of anode materials,<sup>24</sup> in which ionic liquid,  $\text{Li}_2\text{O}$  or  $\text{LiAlSiO}_x$  was used as the electrolyte. Recently, it has been reported that morphology changes of Sn and Si electrodes can be captured in situ during Li ion cycling by liquid cell TEM where  $\text{LiPF}_6/\text{EC}/\text{DMC}$  and  $\text{LiClO}_4/\text{EC}/\text{DMC}$  electrolyte were used. However, the image resolution should be improved.<sup>25,26</sup> So far, it is still a great challenge to study electrochemical processes with the commercial electrolyte for lithium ion batteries, such as  $\text{LiPF}_6$  in organic solvent. This is because such electrolytes have high vapor pressure; thus it is

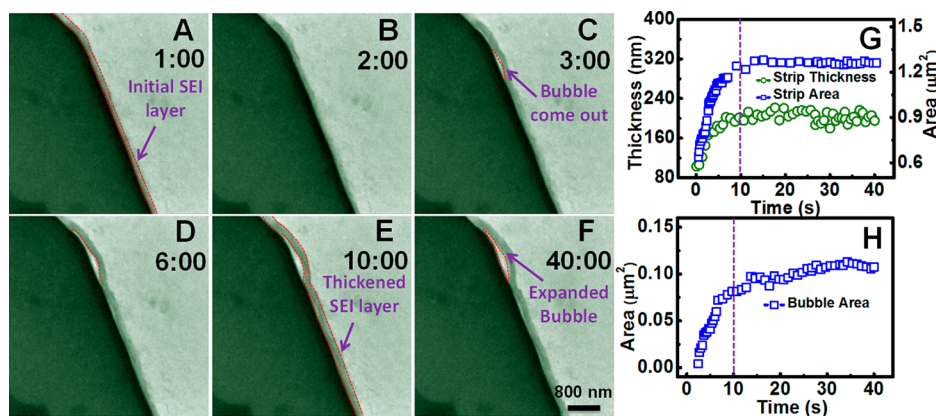


**Figure 3.** (A–F) Time series of TEM images showing the growth of the SEI film with a gas bubble emerged between the gold electrode and the SEI film; (G) thickness and area evolution of an SEI layer; (H) area change of bubble as a function of time during cyclic voltammetry in the voltage range of 4 to 0 V at scan rate of 0.1 V/s.

difficult to handle, and lithium has low contrast during TEM imaging through the membrane window.

Here, utilizing our newly designed electrochemical liquid TEM cells, we observed electrochemical lithiation of Au electrode, dendritic growth of crystalline lithium structure, and the subsequent stripping of lithium and thinning of Li–Au layer under the applied cyclic voltammetry. In addition, we also captured the formation of SEI layer on the other side of the electrode, which is highly valuable to the understanding of correlation between cyclic stability and the passivating film formed during the charge–discharge process in real lithium ion batteries.

Figure 1 is a schematic illustration of the real time observation of electrochemical reaction using the electrochemical liquid cell. The details on biasing liquid cell fabrication have been included in the Supporting Information (SI). The liquid electrolyte was loaded into the biasing cell through the reservoirs. Liquid flows into the cell by capillary force. After liquid loading, we used two pieces of Cu foil to cover the two reservoirs and sealed the liquid cell using epoxy. The sealed cell was put into our homemade TEM holder, and the gold wires bonded on the electrode pads of the biasing cell were connected to the electric pads at the tip of electrochemical holder, as shown in Figure 1A. Thus, an electric bias can be applied through an electrochemical workstation, which was connected to the electric pads through copper wires. Under the applied cyclic voltammetry (Figure 1B), the detailed electrochemical reactions can be monitored in situ. In the current setup, we can observe both sides of the electrodes in the viewing window. SEI formation, Li dendrite growth, and Li–Au reaction on the electrodes have been observed. We first apply cyclic voltammetry with voltage range of 0 to –3 V (scan rate of 0.1 V/s) on the Au electrodes in the electrochemical liquid cell. Either the right electrode (RE) or the left electrode (LE) or both electrodes can be monitored by in situ TEM (Figure 1C). Figure 2A–J shows the sequential images representing the early stage of electrolyte decomposition, lithiation of gold electrode, and the subsequent growth and dissolution of lithium dendrites (also see Movie S1); Figure 1K shows the corresponding applied electrical potential and measured electrical current from frame A to frame J. Initially, surrounded by commercial battery electrolyte 1 M LiPF<sub>6</sub> in EC–DEC (ethylene carbonate/diethyl carbonate in a 1:1 volume ratio), the Au electrode appears to be smooth without obvious

reaction until 27 s (Figure 2A). When cyclic voltammetry is ramped at 0.1 V/s in the negative direction down to –2.75 V, some tiny bubbles (highlighted by purple arrows in Figure 2B) show up indicating the generation of gaseous products, likely PF<sub>5</sub>. At room temperature, an equilibrium exists:<sup>4</sup>



Instantaneously, lithium ions react with an Au electrode to form a thin Li–Au alloy layer (highlighted by red arrows in Figure 2C). Then, the reaction front propagates quickly along the electrode's longitudinal direction with an increase of the Li–Au layer thickness. It indicates that there is a volume expansion when Li reacts with an Au electrode to form an intermetallic compound. Besides the propagated Li–Au alloy, a large bubble is generated by continuing to decrease the negative bias on the active Au electrode. When the Li–Au alloy layer thickness increases to 740 nm, the decomposition of LiPF<sub>6</sub>/EC/DEC electrolyte reaches a peak in the form of gas volume (Figure 2D). Dendritic branches nucleate between the two bubbles in the electrolyte (Figure 2E). Subsequently, the lithium dendrites (highlighted by blue arrows) grow rapidly on the Li–Au alloy layer (Figure 2F–G). The lithium dendrite preserves the shape about 1 s, and then localized Li stripping occurs at the tip of dendrite structure when the voltage is swept back from –3 to 0 V. The dendrites can be dissolved by sweeping the voltage back to –2.85 V particularly (Figure 2H). This corresponds to an increased electric current measured by a CHI electrochemical working station (Figure 2K). Eventually, the branches almost disappeared, and the Li–Au alloy thickness was reduced from 775 to 339 nm (Figure 2I). The thickness of Li–Au alloy does not change drastically at the later stage (Figure 2L). Our observation of lithium dendrite growth from the base point of the passivation film is consistent with the previous study.<sup>3</sup> During stripping, the dissolution of plated lithium starts from the tip and the kink points as a reverse process of plating (Figure 2M).<sup>3</sup>

Figure 3 shows the structure evolution of the SEI film grown on left side electrode (also see Movie S2), which is from the reduction of electrolyte. In this experiment, the potential applied between the two electrodes is cyclic voltammetry with a voltage range of 4 to 0 V and a scan rate of 0.1 V/s (Figure S1). It is noted that before this positive sweeping (4 to 0 V) on the right electrode, we already did negative sweep (0 to –3 V) on the right electrode. Therefore, while Li–Au alloying and

lithium dendrite growth proceed on the right electrode, electrolyte oxidation also occurs on the left electrode, and a thin layer of oxidation film (100 nm) can form on the left electrode. To prove that this oxidation film on left electrode did not change with the same applied voltage program, another round of negative sweep (0 to  $-3$  V) was implemented on right electrode, the recorded movie on left electrode shows that the oxidation film preserves the same morphology with no thickness changes. In this case, a thin oxidation layer is deposited on Au electrode with compact contact. No gap between the thin layer and the Au electrode is observed (Figure 3A–B). Subsequently, a gap between the SEI film and the electrode starts to grow (Figure 3C). Generally speaking, when SEI film is formed on the surface of the active electrode, it protects the electrolytic solution and other battery components from undesirable reduction or oxidation. However, during SEI formation with the reaction of active electrode material, gas can be produced.<sup>27</sup> Defects and strain in the SEI film may also contribute to the peeling of SEI from Au electrode. The emerged void expands quickly from 0 to 10:00 s. Then, the growth rate slows down in the time range from 10 to 40 s (Figure 3H), which indicates the gaseous products evolution almost stops when the applied voltage is zero.

The evolution of thickness and projected area of the SEI film with time are shown in Figure 3G. An initial fast growth of SEI film is observed, and the growth rate drops to almost zero when the voltage is decreased to 0 V. Then, the SEI film maintains at the thickness of about 200 nm. This suggests that the electron mobility is low and the rate of SEI film growth is limited by transport of electrons through the film. The observed SEI is consistent with reports of the SEI layer with layer thickness on the order of 100 nm. In these reports,<sup>4,28</sup> two distinct layers with an inner layer of 1.5–2 nm<sup>4,28</sup> and an outer layer of 100 nm were formed.<sup>28</sup> Previous studies suggest that the inner layer is a compact polycrystalline layer including inorganic products of  $\text{Li}_2\text{CO}_3$ , LiF,  $\text{Li}_2\text{O}$ , and LiCl and the outer layer is a porous, amorphous outer layer formed by partially reduced organic products, for example,  $(\text{CH}_2\text{OCO}_2\text{Li})_2$ , ROLi, and  $\text{ROCO}_2\text{Li}$ ,<sup>29,30</sup> where R is an organic group that depends on the solvent. However, we cannot distinguish these two layers by an in situ TEM observation. Based on our experimental results, SEI is not just a reduction of electrolyte, but also oxidizing species on the surface of electrode, which is consistent with previous literature.<sup>4</sup> A further detailed in situ composition analysis of SEI is needed to elucidate the chemical composition and electronic states.

We have also conducted energy dispersive X-ray spectroscopy (EDS) mapping of the reacted right side electrode (Figure 4A–D). The Au, C, and O maps clearly show the elemental distribution of the reacted Au electrode. Some Au materials sparked away from the electrode, which indicates that Au reacts with a lithium ion and forms a Li–Au alloy layer. Here, we need to mention that SEI formation is also expected to occur on the right side electrode where Li–Au alloying proceeds, and we cannot separate these two processes just from image contrast. However, since cyclic voltammetry ramps the potential quickly in the negative direction on the right electrode to  $-3$  V, the severe reaction accompanied with large volume expansion make it clear that the reaction is dominant by Li–Au alloying.

We did parallel ex situ experiments to confirm the composition and crystal structure of the lithiated Au. Using the same biasing cell operated in air, we found that  $\text{Li}_2\text{O}$  can be produced; see the selected area electron diffraction (SAED)

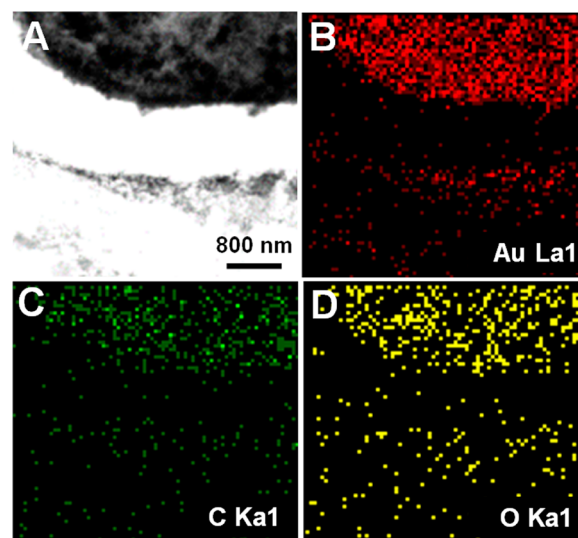


**Figure 4.** (A) TEM image of right side Au electrode electrochemically reacted with lithium ion battery electrolyte in the view window of a liquid cell and the corresponding EDX mapping of (B) Au La1; (C) C Ka1; (D) O Ka1.

pattern with  $\text{Li}_2\text{O}$  (311), (220), and (111) rings in Figure S2A–B. This suggests that lithium can be plated on the electrode during the charge cycles and they were oxidized when the reaction was exposed to air. The same, when a single crystal Au nanowire is used in ex situ conditions, both morphology and crystal structure are observed (Figure S3A–C). The electron diffraction pattern confirms the face-centered cubic (fcc) structure of the Au crystal (space group  $Fm\bar{3}m$ ) (Figure S3C). After cyclic voltammetry, the initially straight Au nanowire becomes a twisted with meandering morphology (Figure S3D). These wavy Au nanowires suggest stress can be generated from deformation of microstructures upon lithiation (Figure S3D–F). Figure S4A–B shows a magnified high-angle annular dark-field imaging (HAADF) of a lithiated Au wire with a meniscus shape. This expanded and warped Au nanowire exhibits a charcoal gray because of heavy lithiation, which is distinctively different from the Au nanowire with light lithiation displaying pale gray. The boundary between the heavy and the light lithiated Au nanowire is marked in red dashed lines. We also observed lots of small grains in the uniform matrix, which suggests that the lithiated Au nanostructure is inhomogeneous with phase segregation. Using a selected area electron diffraction pattern, we further identified the phases of the Li–Au section, as shown in the  $\text{Li}_{15}\text{Au}_4$  phase marked by the red circles (Figure S4C).<sup>31</sup> The blues circles attribute to the original cubic structure of Au (space group  $Fm\bar{3}m$ ). The atomic resolution of Au and Li ordering in an electrochemical treated Au nanowire reveals that a  $\text{Li}_2$  ( $\text{Au}_3\text{Li}$ ) Li–Au structure in coexistence with the pure Au lattice (111) lattice planes<sup>32,33</sup> (Figure S4D). From the spatially resolved EELS spectra (Figure S4E–F), the Au core with Li–Au alloy shell can be achieved. The Li concentration profile can be extracted by integrating the near edge signal from 56 to 65 eV as shown in Figure S4F. The poor jump ratio and low cross section of the Au O edge as compared to these of Li K edge allow us to ignore the contribution from Au in this energy range (Figure S5). We can see the Au concentration is almost the same without obvious deviation along the red dashed line of the cross section of the Au nanowire. However, the Li concentration is lower in the

center of the Au wire, indicating that the electrochemical lithiation starts from the surface of the Au wire and then propagates toward the core.

It is noted that, although we have accomplished the real time imaging of electrochemical reactions in commercial electrolyte for lithium ion batteries using TEM, there are still drawbacks in the current setup. For instance, since lithium metal source was lacking inside the liquid cell to supply the consumed lithium ions during reactions, it is expected that the concentration of Li ions in the electrolyte changes during the reaction. The total lithium consumption in the electrolyte has been estimated (SI). However, such changes do not drastically affect the key electrochemical processes. We have observed SEI formation, lithium dendrite growth, and lithiation and delithiation of electrode materials under an applied cyclic voltammetry, which prove that electrochemical liquid cell can be extremely useful for the study of issues related to lithium ion batteries. For the next electrochemical liquid cell TEM experiments, adding a lithium metal source and an additional reference electrode into the electrochemical liquid cell are necessary for direct comparison between the electrochemical processes under TEM and that in real lithium ion batteries.

Additionally, we would like to point out that electron beam effects are unavoidable in the electrochemical cell TEM experiments since an electron beam is the necessary source for imaging. However, beam effects can be minimized at the reduced electron dose during imaging. Solvated electrons and/or free radicals can be generated as the electron beam passes through the electrolyte in the liquid cell. Generally speaking, the solvated electrons can reduce Li ions in the electrolyte, which could introduce precipitation of Li in the electrolyte solution. However, under current imaging conditions with moderate electron current density (about  $5 \times 10^2$  electrons  $\cdot \text{\AA}^{-2} \cdot \text{s}^{-1}$ ), no obvious precipitation of Li particles or clusters is observed in the solution. To confirm that the lithium deposition and bubble formation are not caused by e-beam irradiation, we also did control experiments, and the results show that without an applied cyclic voltammetry, neither bubble formation nor precipitation of lithium occurs. Despite electron beam effects are complex and difficult to quantify, our extensive experiments have proved that beam effects can be negligible. The SEI formation, Li dendrite growth, and Li–Au reactions can only be achieved when cyclic voltammetry is applied in the electrochemical liquid cell. Therefore, this work on electrochemical reaction at electrode–electrolyte interfaces in  $\text{LiPF}_6/\text{EC}/\text{DEC}$  electrolyte under TEM is valuable for the understanding of electrochemical processes in general.

In summary, an electrochemical liquid cell for in-situ TEM observation is developed via Au lithiation in commercial  $\text{LiPF}_6/\text{EC}/\text{DEC}$  electrolyte. We captured the inhomogeneous lithiation of Au electrode, lithium metal dendritic growth, electrolyte decomposition, and SEI formation that are relevant to real lithium ion batteries. This work is a proof-of-concept that real electrolyte for lithium ion batteries can be used for in situ liquid cell TEM studies. Future work involves adding the third reference electrode, using real electrode materials, and so forth. There is no doubt that electrochemical liquid cell TEM provides a powerful platform for the study of fundamental aspects of electrochemical processes for lithium ion batteries.

## ■ ASSOCIATED CONTENT

### ■ Supporting Information

A description of materials and methods, Figures S1–S5, and two supporting movies. This material is available free of charge via the Internet at <http://pubs.acs.org>.

## ■ AUTHOR INFORMATION

### Corresponding Author

\*E-mail: [hmzheng@lbl.gov](mailto:hmzheng@lbl.gov).

### Notes

The authors declare no competing financial interest.

## ■ ACKNOWLEDGMENTS

We thank Dr. Steve Harris for useful discussions. The experiments were conducted using both MSD TEM facility and a TEAM0.5 microscope at National Center for Electron Microscopy (NCEM) of the Lawrence Berkeley National Laboratory (LBNL), which is supported by the U.S. Department of Energy (DOE) under contract no. DE-AC02-05CH11231. W.L. is supported by National Science Council in Taiwan under contract no. NSC102-2911-I-009-502. H.Z. thanks the support of DOE Office of Science Early Career Research Program. We thank Direct Electron, LP (San Diego, CA) for providing the high speed direct electron camera model DE-12 for movie capture.

## ■ REFERENCES

- (1) Whittingham, M. S. *Chem. Rev.* **2004**, *104*, 4271.
- (2) Arakawa, M.; Tobishima, S.; Nemoto, Y.; Ichimura, M.; Yamaki, J. *J. Power Sources* **1993**, *43*, 27.
- (3) Yamaki, J.; Tobishima, S.; Hayashi, K.; Saito, K.; Nemoto, Y.; Arakawa, M. *J. Power Sources* **1998**, *74*, 219.
- (4) Xu, K. *Chem. Rev.* **2004**, *104*, 4303.
- (5) Verma, P.; Maire, P.; Novak, P. *Electrochim. Acta* **2010**, *55*, 6332.
- (6) Aurbach, D. *J. Power Sources* **2000**, *89*, 206.
- (7) Aurbach, D.; Daroux, M. L.; Faguy, P. W.; Yeager, E. J. *Electrochem. Soc.* **1987**, *134*, 1611.
- (8) Aurbach, D.; Gofer, Y.; Ben-Zion, M.; Aped, P. *J. Electroanal. Chem.* **1992**, *339*, 451.
- (9) Stevens, D. A.; Dahn, J. R. *J. Electrochem. Soc.* **2001**, *148*, A803.
- (10) Owejan, J. E.; Owejan, J. P.; DeCaluwe, S. C.; Dura, J. A. *Chem. Mater.* **2012**, *24*, 2133.
- (11) Zheng, H.; Smith, R. K.; Jun, Y.-w.; Kisielowski, C.; Dahmen, U.; Alivisatos, A. P. *Science* **2009**, *324*, 1309.
- (12) Liao, H.-G.; Cui, L.; Whitelam, S.; Zheng, H. *Science* **2012**, *336*, 1011.
- (13) Williamson, M. J.; Tromp, R. M.; Vereecken, P. M.; Hull, R.; Ross, F. M. *Nat. Mater.* **2003**, *2*, 532.
- (14) Radisic, A.; Vereecken, P. M.; Hannon, J. B.; Searson, P. C.; Ross, F. M. *Nano Lett.* **2006**, *6*, 238.
- (15) de Jonge, N.; Ross, F. M. *Nat. Nanotechnol.* **2011**, *6*, 695.
- (16) Chen, X.; Noh, K. W.; Wen, J. G.; Dillon, S. J. *Acta Mater.* **2012**, *60*, 192.
- (17) Sun, M.; Liao, H.-G.; Niu, K.; Zheng, H. *Sci. Rep.* **2013**, *3*, 3227.
- (18) White, E. R.; Singer, S. B.; Augustyn, V.; Hubbard, W. A.; Mecklenburg, M.; Dunn, B.; Regan, B. C. *ACS Nano* **2012**, *6*, 6308.
- (19) Huang, J. Y.; Zhong, L.; Wang, C. M.; Sullivan, J. P.; Xu, W.; Zhang, L. Q.; Mao, S. X.; Hudak, N. S.; Liu, X. H.; Subramanian, A.; Fan, H. Y.; Qi, L. A.; Kushima, A.; Li, J. *Science* **2010**, *330*, 1515.
- (20) Liu, X. H.; Wang, J. W.; Huang, S.; Fan, F. F.; Huang, X.; Liu, Y.; Krylyuk, S.; Yoo, J.; Dayeh, S. A.; Davydov, A. V.; Mao, S. X.; Picraux, S. T.; Zhang, S. L.; Li, J.; Zhu, T.; Huang, J. Y. *Nat. Nanotechnol.* **2012**, *7*, 749.
- (21) Zhong, L.; Mitchell, R. R.; Liu, Y.; Gallant, B. M.; Thompson, C. V.; Huang, J. Y.; Mao, S. X.; Shao-Horn, Y. *Nano Lett.* **2013**, *13*, 2209.

- (22) McDowell, M. T.; Lee, S. W.; Harris, J. T.; Korgel, B. A.; Wang, C.; Nix, W. D.; Cui, Y. *Nano Lett.* **2013**, *13*, 758.
- (23) Wang, C.-M.; Li, X.; Wang, Z.; Xu, W.; Liu, J.; Gao, F.; Kovarik, L.; Zhang, J.-G.; Howe, J.; Burton, D. J.; Liu, Z.; Xiao, X.; Thevuthasan, S.; Baer, D. R. *Nano Lett.* **2012**, *12*, 1624.
- (24) Liu, X. H.; Huang, J. Y. *Energy Environ. Sci.* **2011**, *4*, 3844.
- (25) Noh, K. W.; Dillon, S. J. *Scr. Mater.* **2013**, *69*, 658.
- (26) Gu, M.; Parent, L. R.; Mehdi, B. L.; Unocic, R. R.; McDowell, M. T.; Sacci, R. L.; Xu, W.; Connell, J. G.; Xu, P.; Abellan, P.; Chen, X.; Zhang, Y.; Perea, D. E.; Evans, J. E.; Lauhon, L. J.; Zhang, J.-G.; Liu, J.; Browning, N. D.; Cui, Y.; Arslan, I.; Wang, C.-M. *Nano Lett.* **2013**, *13*, 6106.
- (27) Christensen, J.; Newman, J. *J. Electrochem. Soc.* **2004**, *151*, A1977.
- (28) Andersson, A. M.; Henningson, A.; Siegbahn, H.; Jansson, U.; Edstrom, K. *J. Power Sources* **2003**, *119*, 522.
- (29) Bar-Tow, D.; Peled, E.; Burstein, L. *J. Electrochem. Soc.* **1999**, *146*, 824.
- (30) Aurbach, D.; Einely, Y.; Zaban, A. *J. Electrochem. Soc.* **1994**, *141*, L1.
- (31) Yuan, L.; Liu, H. K.; Maarroof, A.; Konstantinov, K.; Liu, J.; Cortie, M. *J. New Mater. Electron. Syst.* **2007**, *10*, 95.
- (32) Xin, H. L.; Mundy, J. A.; Liu, Z. Y.; Cabezas, R.; Hovden, R.; Kourkoutis, L. F.; Zhang, J. L.; Subramanian, N. P.; Makharia, R.; Wagner, F. T.; Muller, D. A. *Nano Lett.* **2012**, *12*, 490.
- (33) Lee, Y. J.; Lee, Y.; Oh, D.; Chen, T.; Ceder, G.; Belcher, A. M. *Nano Lett.* **2010**, *10*, 2433.